Journal of Solid State Chemistry 315 (2022) 123476

Contents lists available at ScienceDirect

Journal of Solid State Chemistry

journal homepage: www.elsevier.com/locate/jssc

Superconducting W-C nanopillars fabricated by Ga^+ focused ion beam induced deposition

Pablo Orús [a], Fabian Sigloch [a], Soraya Sangiao [a,b], José María De Teresa [a,b,*]

[a] Instituto de Nanociencia y Materiales de Aragón (INMA), Universidad de Zaragoza-CSIC, 50009, Zaragoza, Spain
[b] Laboratorio de Microscopías Avanzadas (LMA), Universidad de Zaragoza, 50018, Zaragoza, Spain

ARTICLE INFO

2010 MSC:
00–01
99-00

Keywords:
nanofabrication
Focused ion beam
Nanopillar
Superconductivity

ABSTRACT

Ga^+ Focused Ion Beam Induced Deposition (FIBID) is a highly flexible, single-step nanopatterning technique that makes use of a focused beam of Ga^+ ions to locally induce the decomposition of a gaseous precursor material. In combination with the $W(CO)_6$ precursor, Ga^+ FIBID is known to yield a W–C compound that is superconducting below 4.7 K. While most reports on Ga^+ FIBID-grown W–C focus on in-plane patterning, we demonstrate here that growth along the vertical direction may also be achieved by successively stacking a series of individual patterns that get deposited on top of each other. The nanopillars obtained following this procedure reach up to 10 μm in height, and have an aspect ratio of around 50. They exhibit a 68% of metallic W in terms of atomic content, higher than the 40% detected in their in-plane counterparts, while maintaining the superconducting properties. This approach also opens up the possibility of tuning their height and growth angle with respect to the substrate, exhibiting potential applicability in the design of 3D superconducting devices.

1. Introduction

Over the last century, superconducting materials have solidly established themselves as an equally inciting and promising area of study and research in both scientific and engineering fields. When cooled below a critical temperature, T_c, superconductors exhibit zero resistance to the passage of an electrical current. Examples of application of this exciting phenomenon in the macroscale include the generation of high and stable magnetic fields in particle accelerators [1], medical imaging equipment [2], maglev architectures [3], and plasma confinement devices [4], as well as energy storage devices [5]. In the micro- and nanoscale, where downscaling the materials opens up new possibilities and applications [6,7], superconducting materials find application in the design and fabrication of sensors [8–10], quantum computing elements [11,12], and high-frequency electrical filters [13], among others.

The challenge of patterning superconducting materials in the nanoscale is tackled by means of different lithographic, growth, and deposition techniques, each suited to different needs. Some typical examples are optical lithography [14], electron beam lithography [15], and nanoimprint lithography [16]. One notorious approach that represents the main focus of this work is the growth of superconducting nanostructures by *Focused Ion Beam Induced Deposition* (FIBID) – a direct-write, single-step nanofabrication technique that makes use of a focused beam of charged ions (FIB) to locally induce the decomposition of a gaseous precursor [17–19]. As the energetic ions impinge on the sample, they induce the emission of secondary electrons from the substrate, which carry enough energy to crack the adsorbed precursor molecules. They dissociate into a volatile part that is pumped away by the vacuum system of the instrument, and a non-volatile part that permanently remains on top of the substrate, constituting a deposit shaped following the shape (or *pattern*) traced by the beam.

The interest of this technique in the field of superconductors was sparked in 2004, when the occurrence of superconductivity below 4.7 K in the W–C material resulting from the FIBID of the $W(CO)_6$ precursor was first reported [20]. Since then, extensive research on the material has been carried out, including the characterization of its properties and the optimization of the deposition process [21–24], the investigation of vortex phenomena [25–27], and the possibility of tuning its T_c [28,29], among others. A review on the usage of FIBID for the nanopatterning of superconducting nanostructures using $W(CO)_6$ and other precursor materials may be found in Ref. [30].

As it will be further discussed in section 3.1, nanostructures grown by FIBID are first defined as one or multiple patterns – 2D shapes that the user defines for the beam to trace. This approach allows for high growth

* Corresponding author. Instituto de Nanociencia y Materiales de Aragón (INMA), Universidad de Zaragoza-CSIC, 50009, Zaragoza, Spain.
E-mail address: deteresa@unizar.es (J.M. De Teresa).

https://doi.org/10.1016/j.jssc.2022.123476
Received 14 June 2022; Received in revised form 26 July 2022; Accepted 3 August 2022
Available online 13 August 2022

flexibility, since each pattern may be easily tailored to each need. Thus, a significant amount of the reports on FIBID growth relates to in-plane nanostructures, typically with the most complex features occurring in a single plane, and the vertical direction mostly being relegated to the "thickness", as a tunable parameter.

Notwithstanding, the growth of nanostructures by FIBID with characteristic features in all three directions of space, or *3D growth*, makes up for a highly interesting field of study [31,32], even more so in the field of superconductivity. Growing out-of-plane superconducting nanostructures allows for the investigation of phenomena that do not occur in their 2D counterparts, particularly when they are exposed to an external magnetic field: the rise of strong inhomogeneities in the magnetic field components, the appearance of complex patterns in the Meissner currents induced by the field, and the occurrence of emerging phenomena in the vortex dynamics therein [33,34].

Growth of 3D nanostructures using FIBID may be achieved through ingenious operation of the instrument and adequate tuning of the parameters. One of the main challenges resides in an intrinsic property of FIB processing: as the energetic ions in the FIB impinge on the sample, the energy they carry gets redistributed throughout the surface of the sample, both in the form of the aforementioned growth-inducing secondary electron emission, and through material removal or *sputtering*. As such, in all FIBID procedures these two opposite mechanisms compete with each other, and the former must dominate over the latter in order to achieve material growth. This issue can significantly hamper the capability of FIBID to delve into 3D patterning if material is removed equally fast as it is deposited, and it is of ubiquitous nature if relatively heavy Ga^+ ions are used to form the FIB (as it is the case in most current commercial equipment).

Nevertheless, 3D growth of W–C nanostructures by FIBID has been indeed achieved, making use of FIBs fitted with both Ga^+ and (lighter) He^+ ion sources. Li et al. [35] reported in 2007 the usage of a Ga^+ FIB to induce the decomposition of $W(CO)_6$ in the vertical direction, achieving pillar heights of up to 45 μm and retrieving a room-temperature resistivity of the material of 550 μΩ cm, reasonably close to its 2D counterpart (around 200 μΩ cm). In 2010, Romans et al. [36] fabricated 3D freestanding functional pickup loops coupled to Nb SQUIDs by W–C Ga^+ FIBID, constituted of two locally-tilted pillars with diameters of around 200 nm, enclosing an effective area of 1.6 μm. These structures showed T_c ~5.2 K and a normal state resistivity in the order of 100 μΩ cm. Córdoba et al. have recently reported the usage of He^+ FIBID in the growth of 3D W–C nanostructures, namely hollow vertical nanowires [37] and nanohelices [38]. The former, grown up to around 7 μm in height, showed T_c ~6.4 K and exhibited a central columnar void arising as a consequence of the fine deposition/milling interplay taking place during He^+ FIBID. The helices were grown with heights in the 4 μm–7 μm range with different geometries, and exhibited T_c values in the 6.2 K–7.0 K range.

Achieving precise control in the out-of-plane growth of superconducting nanostructures with the flexibility provided by FIBID may represent a powerful tool for the fabrication of three-dimensional superconducting nanocircuits, which can find application in sensing and in other superconducting quantum technologies. On that basis, in this work we report the nanopatterning of superconducting 3D W–C tilted nanopillars by Ga^+ FIBID. By sequentially scanning a series of circle-shaped patterns positioned in close proximity to each other, we achieve vertical growth at variable angles. A characterization study of the electrical, compositional, and microstructural properties reveals a superconducting transition near T_c ~4.7 K, an atomic tungsten content of around 65%, and an amorphous microstructure. Remarkably, and compared to in-plane W–C deposits grown by Ga^+ FIBID, the W content is higher (68% compared to 40%), and the room-temperature resistivity is generally lower.

2. Methods

The samples were grown on silicon pieces topped with a thermally-grown, 300 nm-thick SiO_2 layer. These substrates had been previously patterned via optical lithography with a supporting framework of 100 nm-thick Ti contact pads, to be used in the electrical characterization of the pillars.

2.1. Nanofabrication

The nanopillars were fabricated in a commercial Thermo Fisher *Helios 600 Dual Beam* FIB/SEM microscope, fitted with a liquid metal ion source-based Ga^+ FIB, an electron column acting as a scanning electron microscope (SEM), and a gas injection system (GIS) for precursor delivery onto the substrate surface.

The deposition was performed at the conventional working height of the microscope, referred to as the *eucentric point*, located at the coincidence focus point of the FIB and the SEM. The $W(CO)_6$ GIS was positioned 50 μm away and 100 μm away of the irradiation spot in the in-plane and vertical distances, respectively. The vacuum level of the process chamber was kept at a base pressure of 1×10^{-6} mbar, and it was raised to 1×10^{-5} mbar during gas delivery.

The nanopillars were grown using an acceleration voltage of 30 kV, an ion beam current of 1.5 pA, and a volume per dose of 8.2×10^{-2} $\mu m^3 nC^{-1}$. The specifics on the pattern arrangement employed to achieve 3D growth are discussed below in section 3.1.

2.2. Characterization

For the purposes of the present study, nanopillars may not be adequately characterized while standing upright, since both transmission electron microscopy (TEM) and four-probe electrical characterization require the samples to be lying flat on the substrate. To that end, the nanopillars were toppled using an Oxford Instruments *Ommniprobe 200* nanomanipulator mounted in a Thermo Fisher *Helios 650 Dual Beam* microscope, functionally equivalent to the previously described *Helios 600*.

After toppling, the nanopillars were electrically connected to the supporting Ti pads by growing four Pt nanowires via FIBID of the $CpPtMe_3$ precursor, known to be suitable for this purpose [24,39]. The room-temperature resistivity was measured by taking four-probe current-voltage measurements within the same instrument, making use of a commercial Kleindiek Nanotechnik microprobe station connected to a Keithley Instruments 6221 DC current source and a 2182A nanovoltmeter by means of a chamber feedthrough.

The low-temperature electrical measurements were performed in a commercial Quantum Design *Physical Property Measurement System* instrument, cooling the samples down to 2 K. The Ti pads on the substrates were electrically connected to the instrument sampleholder by ultrasonic wirebonding.

The composition and microstructure of the nanopillars were assessed by means of TEM. The chemical composition was evaluated using scanning TEM (STEM) techniques: energy-dispersive X-ray spectroscopy (EDS) and high angle angular dark field imaging (HAADF) in a commercial FEI *TITAN Low-Base* instrument. The microstructure was investigated by taking high resolution TEM images (HRTEM) in a commercial FEI *TITAN*^{3} microscope.

3. Results

3.1. Growth and geometry

In-plane FIBID nanostructures are typically grown by designing one or multiple *patterns* in the form of geometrical shapes that the beam will trace during irradiation, resulting in the deposition of patterns exhibiting those shapes [19]. The thickness of the deposits is tuned by adjusting the ion dose: increasing the deposition time (on which the ion dose depends) results in the beam scanning over previously-grown material, the surface of which is constantly being replenished by gaseous precursor molecules

delivered by the GIS. The decomposition of these precursor molecules induces the growth on top of the already-deposited material, which allows for thickness modulation of the deposits.

As the FIB impinges on the sample, the energy transfer between the energetic ions and the atoms in the substrate results in the production of backscattered ions and in the emission of secondary electrons. The latter decompose the adsorbed precursor molecules, promoting growth. The emission of these secondary electrons occurs in a finite area larger than the spot of direct irradiation. Thus, when designing geometries near the patterning resolution limit of the specific ionic species, deposited features are generally greater in size than the nominal dimensions of the patterns employed to grow them [40].

This effect can be exploited to indirectly favor vertical growth of the material by arranging a series of identical circle-shaped patterns with reduced nominal diameter (*i.e.*, comparable to the resolution limit of the instrument) in a straight line (Fig. 1a). With the actual size of the grown features significantly exceeding that of the patterns, by sequentially scanning the patterns one at a time, newer deposits grow on top of previously-deposited features, with the overall structure growing along the vertical direction following the direction of the scan (Fig. 1b). Eventually, the line of individual, separated circles yields a tilted nanopillar, intuitively similar to a pile of stacked poker chips (Fig. 1c).

The height of the nanopillar (*i.e.*, its length along the longitudinal axis) is determined by the number of circular patterns. Each individual circle has a nominal diameter of 15 nm and is patterned with an ion dose of 125 nC μm^{-2}, amounting to a deposition time of 7 s per circle. The actual diameter of the pillar, as measured by TEM imaging (later presented in section 3.2), falls around 200 nm. With the nominal size of the pattern already below the patterning resolution limit of the instrument (of around 20 nm for Ga^{+} ions in the best possible conditions [19]) the large size difference between the pattern and the deposits is accounted for by both extrinsic and intrinsic effects. Due to the relatively long exposure time, extrinsic effects related to FIB drifting of mechanical and thermal origin can occur. FIBID-intrinsic effects that account for pillar

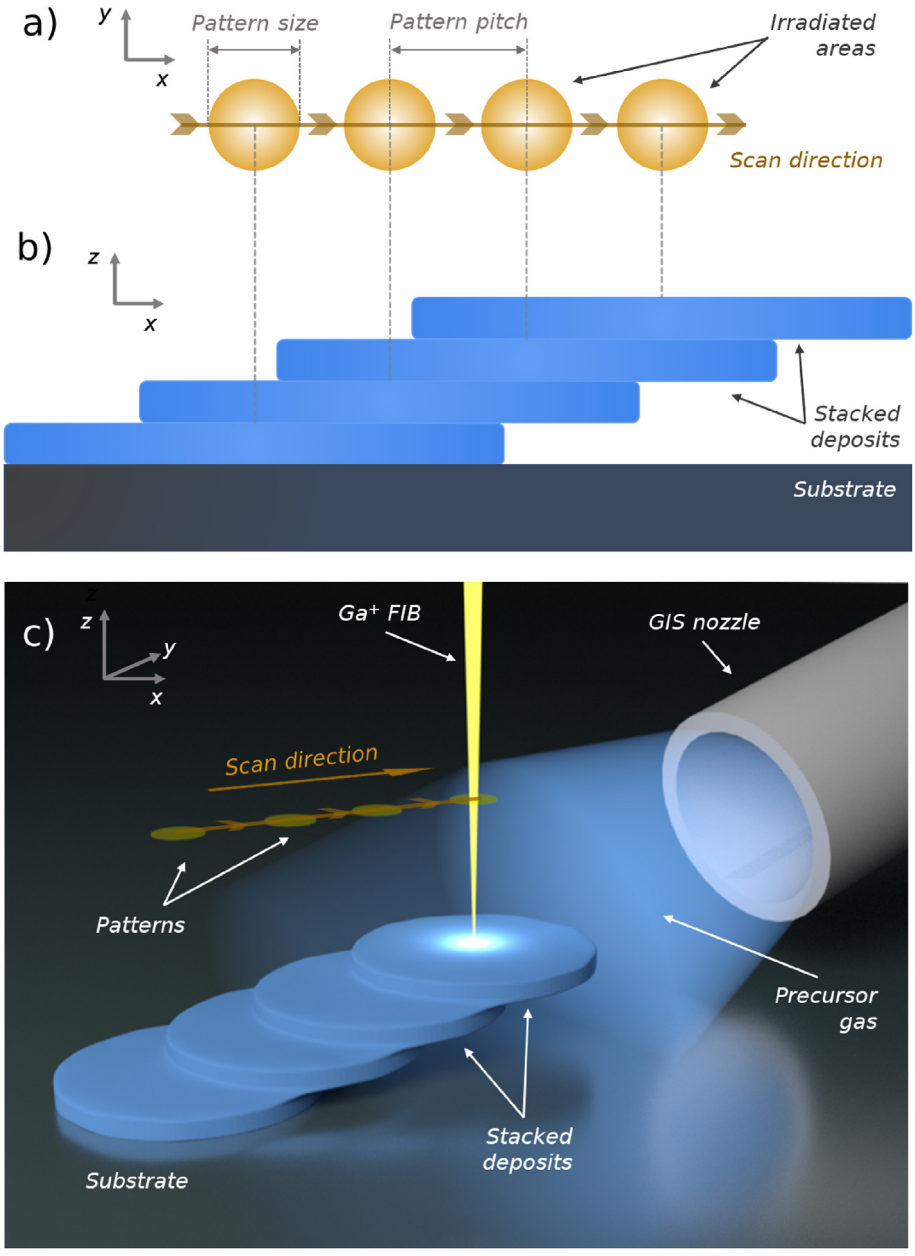

Fig. 1. Scheme of the planar pattern arrangement utilized to induce the 3D growth of the nanopillars (not to scale, *x* direction exaggerated). **(a)** Top view of the in-plane (*xy*) pattern layout. **(b)** Side view of the growth along the vertical direction (*z*) by consecutive stacking of adjacent patterns. **(c)** Procedure overview.

widening are related to forward ion scattering, to ion backscattering in the growing structure, and to the production of secondary electrons in a region separated from the primary ion incidence point [41].

The separation between consecutive patterns or pattern pitch determines the growth angle. The pitch may also be expressed in terms of the overlap between successive patterns, with an overlap of 100% corresponding to a full superposition of the two, and negative values of the overlap indicating a pitch greater than the pattern size.

The influence of the overlap was assessed by growing three nanopillars consisting of 37 identical circular patterns with varying pitch (Fig. 2). With a complete overlap of consecutive patterns, the stacked patterns grow vertically with a tilt angle α of 0°, an overlap of 50% yields $\alpha \sim 4°$, and an overlap of 0% enhances α up to $\sim 10°$. Vertical growth is not achieved at greater values of the pitch, suggesting that the individual patterns might be too far apart from each other to properly stack. However, the tilt angle may be further tuned by adjusting the relative inclination between the ion beam and the substrate: while the conventional beam incidence at 90° with respect to the substrate promotes vertical growth, non-normal FIB incidence angles direct the 3D growth along the corresponding direction [42].

Vertical growth was observed up to pillar heights of 10 μm (Fig. 3a), whose growth time amounted to around 11 min. For the electrical and TEM characterization studies, the pillars were toppled and electrically contacted to the supporting electrical pads (Fig. 3b), as described in section 2.2.

3.2. Microstructure and composition

The compositional and microstructural analysis of the samples was carried out by following standard TEM sample preparation procedures to extract lamellae from the toppled pillars.

As observed by HRTEM imaging (Fig. 4a), the nanopillars exhibit a cross-sectional area roughly elliptical in shape. The deviance from the originally circular shape of the patterns can be ascribed to the beam drifting during irradiation and to "bevel" effects related to the cut performed during lamellae preparation, slightly deviated from an ideal transversal cut.

Two very distinct constituting layers can be identified in the cross-section of the nanopillar: a central core with main axes of around 150 nm and 100 nm in size, and an outer, spatially-anisotropic layer that encloses it. No crystalline order is detected in either layer, contrary to the crystal lattice observed in W–C nanopillars grown by He^+ FIBID [37].

STEM-HAADF images of the cross-sectional view of the nanopillars (Fig. 4b) and the subsequent EDS analysis (Fig. 4c and d) indicate that the two layers are significantly distinct in terms of composition, with the core exhibiting a large metallic content, and the outer layer showing a much higher oxygen content.

In the core, EDS quantification indicates an averaged composition ratio (in terms of atomic percentage) of 69 ± 4% W, 17 ± 1% O, and 14 ± 3% C. The same analysis carried out in an equivalent sample yields a similar ratio of 67 ± 7% W, 13 ± 4% O, and 20 ± 4% C. Remarkably, in either case no significant amount of Ga is detected, within the resolution limit of the technique.

On the other hand, the composition of the outer layer is mostly dominated by oxygen, which can be attributed to an oxidation of the pillar due to its exposure to ambient air during sample handling and transportation. The composition ratios for the pictured and backup samples change to 22 ± 2% W, 75 ± 4% O, and 3 ± 2% C; and 22 ± 3% W, 65 ± 2% O, and 13 ± 6% C. Again, no significant amount of Ga is detected from the EDS analyses.

Such compositional differences with in-plane nanostructures were also observed in the vertical growth of W–C hollow nanopillars by He^+ FIBID [37]. A plausible hypothesis for their occurrence is related to the changes in the growth procedure – while substrate-emitted secondary electrons are the main drive for in-plane growth; during 3D deposition the growth-inducing secondary electrons are emitted from previously-grown material. Since the substrate and grown material are generally different from each other from a compositional and structural point of view, the number of secondary electrons they emit upon FIB irradiation is also expected to be different. Moreover, thermal effects during growth of 3D structures by FIBID can take place, similarly to the heating effects observed during the growth of 3D structures by focused electron beam induced deposition [43]. Eventually, these different emission yields may lead to changes in the efficiency of precursor decomposition, which modifies the composition of the grown material. In addition, the absence of Ga in the compositional analysis indicates that Ga implantation seems to occur mostly on the substrate, and not on previously grown material.

3.3. Electrical characterization

The electrical measurements were carried out in nanopillars grown with a tilt angle of 4°. The linearity of the current-voltage characteristics retrieved from two nanopillars at 300 K (Fig. 5) indicates that they exhibit ohmic behavior at that temperature. Assuming that conductivity takes place at the metallic core of the nanopillars, the observed values of resistance yield approximated resistivity figures of around 70 μΩ cm, about half the value of those typically detected in in-plane W–C Ga^+ FIBID nanostructures, in good agreement with the higher metallic content of these pillars compared to in-plane structures.

The extent of the oxidation process, and thus, the actual size of the metallic core during the electrical characterization, retrieved prior to the TEM study, is unknown. Therefore, the previous figure represents a minimum value for the resistivity, assuming that the size of the oxidized

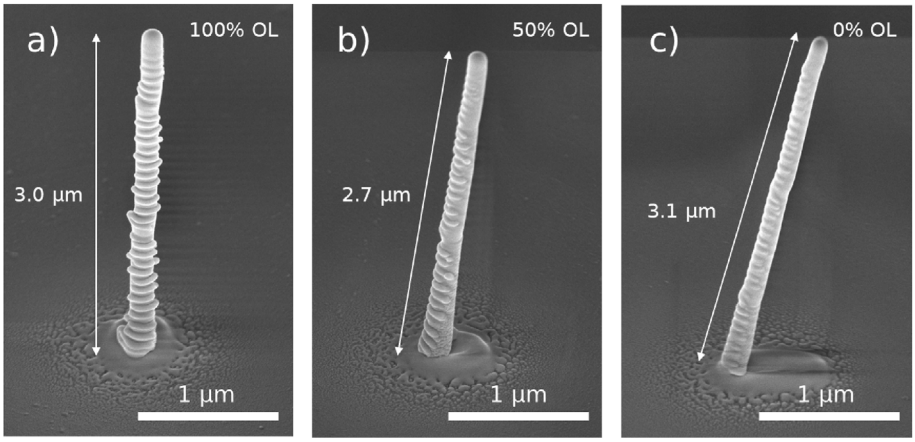

Fig. 2. Influence of the pattern overlap (OL) on the tilt angle of the nanopillars, α. **(a)** 100% OL, $\alpha \sim 0°$, **(b)** 50% OL, $\alpha \sim 4°$, **(c)** 0% OL, $\alpha \sim 10°$.

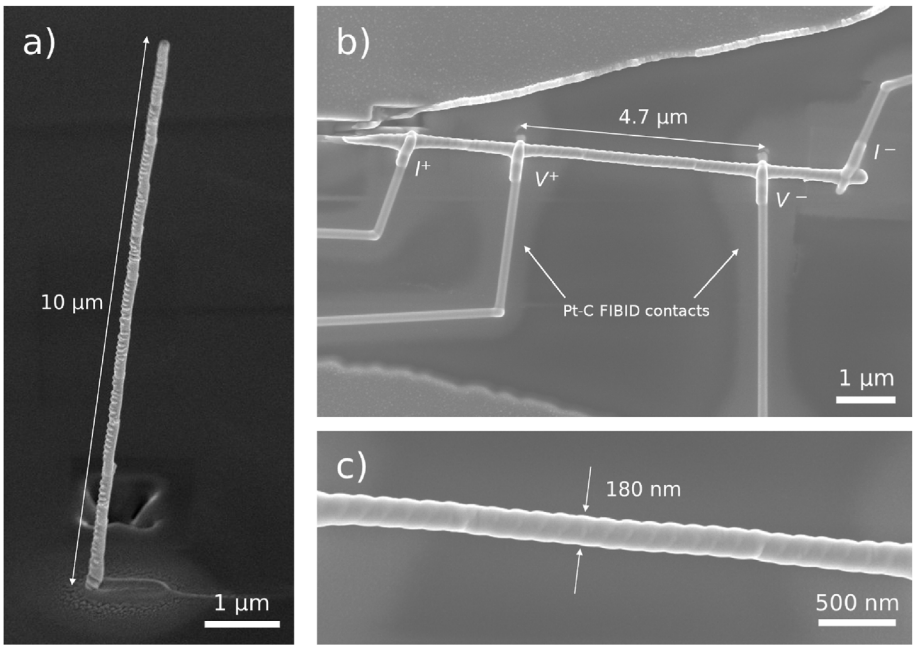

Fig. 3. **(a)** 10 µm-high nanopillar grown with an overlap of 50%. **(b)** Toppled nanopillar electrically connected to the supporting Ti-pads by Pt–C FIBID contacts. The current ($I^{+/-}$) and voltage ($V^{+/-}$) polarization points are indicated. **(c)** Higher-magnification view of the central area of the pillar.

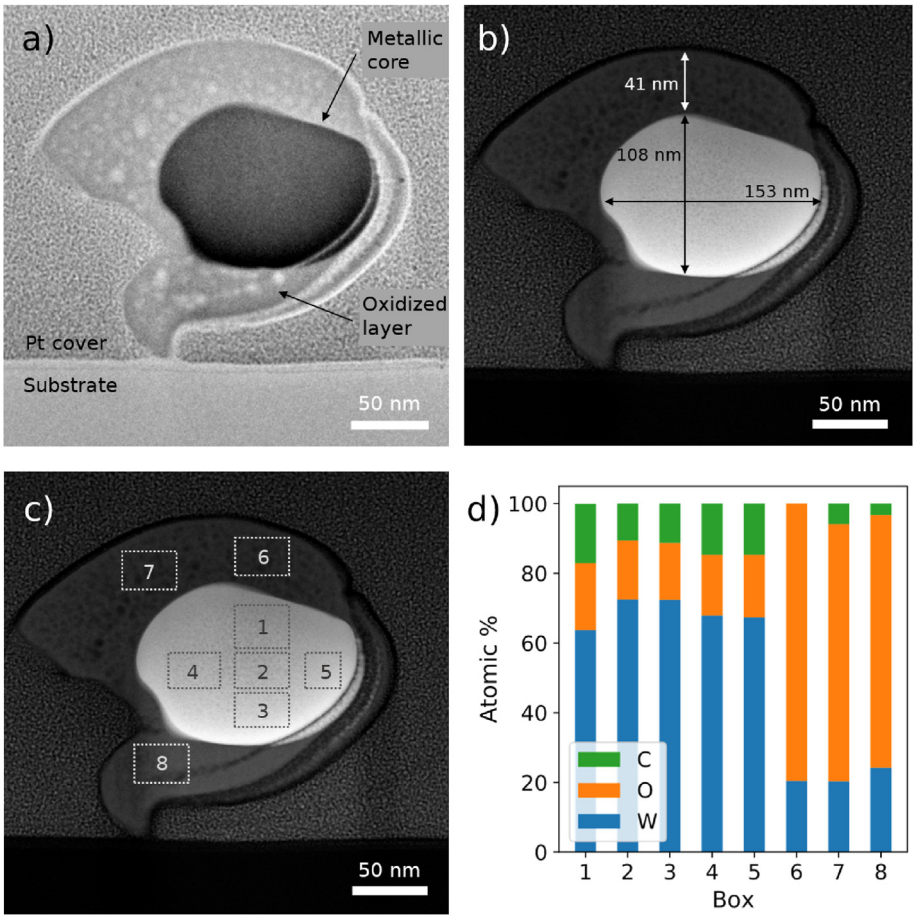

Fig. 4. TEM-based structural and compositional analysis of the samples. Each TEM image shows a cross-sectional view of a toppled pillar. **(a)** HRTEM image. **(b)** STEM-HAADF image, with characteristic lengths indicated. **(c)** and **(d)** EDS compositional quantification of the indicated areas.

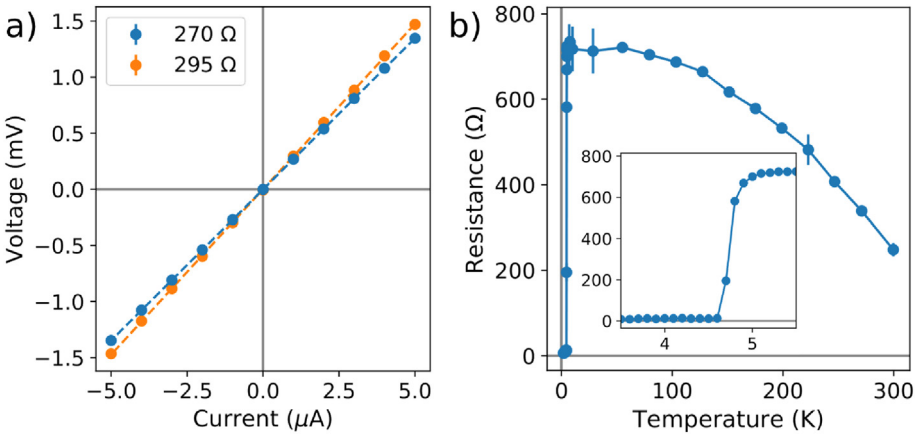

Fig. 5. **(a)** Current-voltage characteristic of two nanopillars at 300 K. **(b)** Temperature dependence of the resistance of a nanopillar. The inset shows a zoomed-in view of the superconducting transition occurring at $T_c = 4.7$ K.

layer did not significantly change after the electrical characterization, prior to TEM imaging. Conversely, the maximum value the resistivity may take is that for which the whole structure is assumed to be contributing to the conduction, corresponding to a value of around 200 μΩ cm, similar to the value retrieved in in-plane W–C Ga^+ FIBID nanostructures. The actual value of the nanopillar resistivity during the electrical measurements must therefore fall within these bounds.

By cooling the samples down to 2 K, a transition to the superconducting state is observed at T_c ~4.7 K (defining T_c as the temperature value at which the resistance of the material takes half the value it takes in the normal state, here defined at 10 K). A slight negative dependence of the resistance with temperature is detected before the superconducting transition, same as that observed in in-plane W–C nanowires grown by Ga^+ FIBID [22], and is ascribed to the inherent disorder existing in this type of materials.

4. Discussion and outlook

The proposed method provides with yet another alternative approach for the exploitation of the flexibility of FIBID to grow of out-of-plane structures, comparable to those already carried out in this material with this ionic species [35,36], as well as those performed in niobium (Table 1).

Despite the significant compositional differences between the 3D nanopillars and the in-plane nanostructures nanopatterned using the same technique, the observed value of T_c is remarkably close to that observed in in-plane nanostructures [20, 24]. On the other hand, the room-temperature resistivity does exhibit a significant decrease in comparison with the in-plane counterparts.

Furthermore, the 3D W–C nanowires prepared by He^+ FIBID [37,38] do exhibit a similar amount of W, yet their room-temperature resistivity is higher than that of in-plane Ga^+ FIBID nanowires. A WC_{1-x} crystalline structure is detected in those nanowires, which might account for the increase in T_c characteristic to the He^+ FIBID approach. As discussed in Ref. [30], the origin of the superconductivity in W–C deposits is a matter of debate, but it is likely that two different superconducting phases are possible depending on the exact growth conditions.

The foreseeable perspectives and applications for this growth procedure include the nanopatterning and design of tilted 3D superconducting nanodevices. One possible modification of the proposed procedure would be to include non-monotonous separation and orientation of the patterns in the array, potentially enabling for changing the tilt and orientation of the 3D structure at intermediate points. In addition, and as previously anticipated, by performing the irradiation with non-normal FIB incidence, the tilt angle could potentially be increased above the limit set by the pitch. One specific potential application of the method would be to grow superconducting nanopillars in cantilevers to serve as superconducting sensors, in a similar way as the already-reported magnetic tips grown via focused electron beam induced deposition [45] and the W–C freestanding pickup loops grown by Ga^+ FIBID [36].

Table 1
Comparison between the results of the present work, other FIBID approaches to grow W–C, and Nb growth by 3D FIBID.

Material	Tungsten			Niobium
FIBID approach	3D Ga^+	2D Ga^+	3D He^+	3D Ga^+
Met. cont. (atomic)	68%	40%	72%	–
ρ_{RT} (μΩcm^{-1})	70–200	200	400–460	380
T_c (K)	4.7	4.0–5.0	6.2–7.1	11.4
Microstructure	Amorphous	Amorphous	WC_{1-x}	fcc
References	Present work	[20,24]	[37,38]	[44]

5. Conclusions

To conclude, we have presented a FIBID nanopatterning approach based on the sequential scanning of overlapping patterns to achieve 3D growth of superconducting W–C nanopillars obtained by Ga^+ FIB decomposition of the $W(CO)_6$ precursor. By successive stacking of individual patterns, growth is promoted in a vertical direction, with the possibility of tuning the tilt angle up to 10° with normal FIB incidence. The pillars are roughly 200 nm in diameter and reach heights of up to 10 μm.

TEM characterization of the pillars reveals an atomic W content of around 68%, significantly higher than the 40% detected in in-plane Ga^+ FIBID W–C nanostructures. Contrary to 3D He^+ FIBID nanostructures, the 3D nanopillars grown by Ga^+ FIBID lack crystallinity.

The electrical characterization of the samples indicates that the pillars exhibit a remarkably low room-temperature resistivity in the range of 70 μΩcm to 200 μΩcm, and a critical temperature of 4.7 K. The room-temperature resistivity is lower than that retrieved in both in-plane Ga^+ FIBID nanowires and 3D He^+ FIBID nanopillars, while the critical temperature matches that of in-plane Ga^+ FIBID nanowires, and is lower than that retrieved in 3D He^+ FIBID nanopillars.

The flexibility of the FIBID procedure, which allows for further tilting of the stage, complex pattern arrangements and deposition parameter tuning, makes of the technique a viable and promising approach for the nanopatterning of 3D superconductors.

Declaration of competing interest

The authors declare that they have no known competing financial

interests or personal relationships that could have appeared to influence the work reported in this paper.

Data availability

Data will be made available on request.

Acknowledgments

The microscopy works have been conducted in the Laboratory for Advanced Microscopies (LMA), at the Institute of Nanoscience and Materials of Aragón (INMA)—University of Zaragoza. Authors acknowledge the LMA-INMA for offering access to their instruments and expertise, and particularly thank L. Casado for her assistance with the nanomanipulation procedures and the electrical measurements. Authors acknowledge the Physical Measurements Service from Servicio General de Apoyo a la Investigación (SAI)—University of Zaragoza.

This research was supported by the European Commission under H2020 FET Open grant 'FIBsuperProbes' (number 892427), the grant PID2020-112914RB-I00 funded by MCIN/AEI/10.13039/501100011033, from CSIC through projects PIE202060E187 and Research Platform PTI-001, and by Gobierno de Aragón through the grant E13_20R with European Social Funds (Construyendo Europa desde Aragón).

The authors have written this article in recognition of the contributions of Prof. M. A. Alario to the scientific development in Spain.

References

[1] L. Rossi, The LHC superconducting magnets, in: Proceedings of the 2003 Particle Accelerator Conference vol. 1, IEEE, 2003, pp. 141–145.
[2] R. Aarnink, J. Overweg, Magnetic resonance imaging, a success story for superconductivity, EuroPhys. News 43 (4) (2012) 26–29.
[3] P. Bernstein, J. Noudem, Superconducting magnetic levitation: principle, materials, physics and models, Supercond. Sci. Technol. 33 (3) (2020), 033001.
[4] M. Huguet, The ITER magnet system, Fusion Eng. Des. 36 (1) (1997) 23–32.
[5] D. Larbalestier, A. Gurevich, D.M. Feldmann, A. Polyanskii, High-T_c superconducting materials for electric power applications, in: Materials for Sustainable Energy: A Collection of Peer-Reviewed Research and Review Articles from Nature Publishing Group, World Scientific, 2011, pp. 311–320.
[6] T.A. Saleh, Nanomaterials: classification, properties, and environmental toxicities, Environ. Technol. Innovat. 20 (2020), 101067.
[7] T.A. Saleh, Global trends in technologies and nanomaterials for removal of sulfur organic compounds: clean energy and green environment, J. Mol. Liq. (2022), 119340.
[8] C.M. Natarajan, M.G. Tanner, R.H. Hadfield, Superconducting nanowire single-photon detectors: physics and applications, Supercond. Sci. Technol. 25 (6) (2012), 063001.
[9] D. Koelle, R. Kleiner, F. Ludwig, E. Dantsker, J. Clarke, High-transition-temperature superconducting quantum interference devices, Rev. Mod. Phys. 71 (3) (1999) 631.
[10] A. Shurakov, Y. Lobanov, G. Goltsman, Superconducting hot-electron bolometer: from the discovery of hot-electron phenomena to practical applications, Supercond. Sci. Technol. 29 (2) (2015), 023001.
[11] D. Vion, A. Aassime, A. Cottet, P. Joyez, H. Pothier, C. Urbina, D. Esteve, M.H. Devoret, Manipulating the quantum state of an electrical circuit, Science 296 (5569) (2002) 886–889.
[12] I. Chiorescu, Y. Nakamura, C.M. Harmans, J. Mooij, Coherent quantum dynamics of a superconducting flux qubit, Science 299 (5614) (2003) 1869–1871.
[13] J. Martinez, Y. Hijazi, M. Brzhezinskaya, A. Bogozi, J. Noel, Y.A. Vlasov, G.L. Larkins Jr., Design, simulation, and fabrication of a mems switched superconducting microstrip hairpin filter, Phys. C Supercond. 466 (1–2) (2007) 101–105.
[14] F. Vallès, A. Palau, V. Rouco, B. Mundet, X. Obradors, T. Puig, Angular flux creep contributions in $YBa_2Cu_3O_{7-\delta}$ nanocomposites from electrical transport measurements, Sci. Rep. 8 (1) (2018) 5924.
[15] E. Monticone, C. Portesi, S. Borini, E. Taralli, M. Rajteri, Superconducting MgB_2 nanostructures fabricated by electron beam lithography, IEEE Trans. Appl. Supercond. 17 (2) (2007) 222–224.
[16] L. Zhao, Y. Jin, J. Li, H. Deng, H. Li, K. Huang, L. Cui, D. Zheng, Fabrication of Nb superconducting nanowires by nanoimprint lithography, IEEE Trans. Appl. Supercond. 25 (3) (2014), 2200605.
[17] L.A. Giannuzzi, et al., Introduction to Focused Ion Beams: Instrumentation, Theory, Techniques and Practice, Springer Science & Business Media, 2004.
[18] I. Utke, P. Hoffmann, J. Melngailis, Gas-assisted focused electron beam and ion beam processing and fabrication, J. Vac. Sci. Technol. B: Microelectro. Nanometer Struct. Process. Measure. Phenomena 26 (4) (2008) 1197–1276.
[19] P. Orús, R. Córdoba, J.M. De Teresa, Focused ion beam induced processing, in: Nanofabrication, 2053-2563, IOP Publishing, 2020, 5–1 to 5–58.
[20] E. Sadki, S. Ooi, K. Hirata, Focused-ion-beam-induced deposition of superconducting nanowires, Appl. Phys. Lett. 85 (25) (2004) 6206–6208.
[21] I. Luxmoore, I. Ross, A. Cullis, P. Fry, J. Orr, P.D. Buckle, J. Jefferson, Low temperature electrical characterisation of tungsten nano-wires fabricated by electron and ion beam induced chemical vapour deposition, Thin Solid Films 515 (17) (2007) 6791–6797.
[22] J. M. De Teresa, A. Fernandez-Pacheco, R. Cordoba, J. Sese, R. Ibarra, I. Guillamon, H. Suderow, S. Vieira, Transport properties of superconducting amorphous W-based nanowires fabricated by focused-ion-beam-induced-deposition for applications in Nanotechnology, MRS Online Proceedings Library (OPL) 1180 (2009) 1180-CC04-09.
[23] W. Li, J. Fenton, C. Gu, P. Warburton, Superconductivity of ultra-fine tungsten nanowires grown by focused-ion-beam direct-writing, Microelectron. Eng. 88 (8) (2011) 2636–2638.
[24] R. Córdoba, T. Baturina, J. Sesé, A.Y. Mironov, J. De Teresa, M. Ibarra, D. Nasimov, A. Gutakovskii, A. Latyshev, I. Guillamón, et al., Magnetic field-induced dissipation-free state in superconducting nanostructures, Nat. Commun. 4 (2013) 1437.
[25] I. Guillamón, H. Suderow, A. Fernández-Pacheco, J. Sesé, R. Córdoba, J. De Teresa, M. Ibarra, S. Vieira, Direct observation of melting in a two-dimensional superconducting vortex lattice, Nat. Phys. 5 (9) (2009) 651–655.
[26] I. Guillamón, R. Córdoba, J. Sesé, J.M. De Teresa, M.R. Ibarra, S. Vieira, H. Suderow, Enhancement of long-range correlations in a 2d vortex lattice by an incommensurate 1d disorder potential, Nat. Phys. 10 (11) (2014) 851–856.
[27] R. Córdoba, P. Orús, Ž.L. Jelić, J. Sesé, M.R. Ibarra, I. Guillamón, S. Vieira, J.J. Palacios, H. Suderow, M.V. Milošević, et al., Long-range vortex transfer in superconducting nanowires, Sci. Rep. 9 (1) (2019), 12386.
[28] J. Dai, K. Onomitsu, R. Kometani, Y. Krockenberger, H. Yamaguchi, S. Ishihara, S. Warisawa, Superconductivity in tungsten-carbide nanowires deposited from the mixtures of $W(CO)_6$ and $C_{14}H_{10}$, Japanese, J. Appl. Phys. 52 (7R) (2013), 075001.
[29] F. Porrati, L. Keller, C. Gspan, H. Plank, M. Huth, Electrical transport properties of Ga irradiated W-based granular nanostructures, J. Phys. Appl. Phys. 50 (21) (2017), 215301.
[30] P. Orús, F. Sigloch, S. Sangiao, J.M. De Teresa, Superconducting materials and devices grown by focused ion and electron beam induced deposition, Nanomaterials 12 (8) (2022) 1367.
[31] M. Esposito, V. Tasco, M. Cuscuna, F. Todisco, A. Benedetti, I. Tarantini, M.D. Giorgi, D. Sanvitto, A. Passaseo, Nanoscale 3D chiral plasmonic helices with circular dichroism at visible frequencies, ACS Photonics 2 (1) (2015) 105–114.
[32] A. Belianinov, M.J. Burch, A. Ievlev, S. Kim, M.G. Stanford, K. Mahady, B.B. Lewis, J.D. Fowlkes, P.D. Rack, O.S. Ovchinnikova, Direct write of 3D nanoscale mesh objects with platinum precursor via focused helium ion beam induced deposition, Micromachines 11 (5) (2020) 527.
[33] V.M. Fomin, O.V. Dobrovolskiy, A Perspective on superconductivity in curved 3D nanoarchitectures, Appl. Phys. Lett. 120 (9) (2022), 090501.
[34] D. Makarov, O.M. Volkov, A. Kákay, O.V. Pylypovskyi, B. Budinská, O.V. Dobrovolskiy, New dimension in magnetism and superconductivity: 3D and curvilinear nanoarchitectures, Adv. Mater. 34 (3) (2022), 2101758.
[35] W. Li, P. Warburton, Low-current focused-ion-beam induced deposition of three-dimensional tungsten nanoscale conductors, Nanotechnology 18 (48) (2007), 485305.
[36] E. Romans, E. Osley, L. Young, P. Warburton, W. Li, Three-dimensional nanoscale superconducting quantum interference device pickup loops, Appl. Phys. Lett. 97 (22) (2010), 222506.
[37] R. Córdoba, A. Ibarra, D. Mailly, J.M. De Teresa, Vertical growth of superconducting crystalline hollow nanowires by He^+ focused ion beam induced deposition, Nano Lett. 18 (2) (2018) 1379–1386.
[38] R. Córdoba, D. Mailly, R.O. Rezaev, E.I. Smirnova, O.G. Schmidt, V.M. Fomin, U. Zeitler, I. Guillamón, H. Suderow, J.M. De Teresa, Three-dimensional superconducting nanohelices grown by He^+-focused-ion-beam direct writing, Nano Lett. 19 (12) (2019) 8597–8604.
[39] K. Gross, J.P. Barragán, S. Sangiao, J. De Teresa, L. Lajaunie, R. Arenal, H.A. Calderón, P. Prieto, Electrical conductivity of oxidized-graphenic nanoplatelets obtained from bamboo: effect of the oxygen content, Nanotechnology 27 (36) (2016), 365708.
[40] C. Sanz-Martín, C. Magén, J.M. De Teresa, High volume-per-dose and low resistivity of cobalt nanowires grown by Ga^+ focused ion beam induced deposition, Nanomaterials 9 (12) (2019) 1715.
[41] P. Alkemade, H. Miro, Focused helium-ion-beam-induced deposition, Appl. Phys. A 117 (4) (2014) 1727–1747.
[42] R. Córdoba, M. Lorenzoni, J. Pablo-Navarro, C. Magén, F. Pérez-Murano, J.M. De Teresa, Suspended tungsten-based nanowires with enhanced mechanical properties grown by focused ion beam induced deposition, Nanotechnology 28 (44) (2017), 445301.
[43] E. Mutunga, R. Winkler, J. Sattelkow, P.D. Rack, H. Plank, J.D. Fowlkes, Impact of electron-beam heating during 3d nanoprinting, ACS Nano 13 (5) (2019) 5198–5213.
[44] F. Porrati, S. Barth, R. Sachser, O.V. Dobrovolskiy, A. Seybert, A.S. Frangakis, M. Huth, Crystalline niobium carbide superconducting nanowires prepared by focused ion beam direct writing, ACS Nano 13 (6) (2019) 6287–6296.
[45] M. Jaafar, J. Pablo-Navarro, E. Berganza, P. Ares, C. Magén, A. Masseboeuf, C. Gatel, E. Snoeck, J. Gómez-Herrero, J.M. De Teresa, et al., Customized MFM probes based on magnetic nanorods, Nanoscale 12 (18) (2020) 10090–10097.